RSC Advances

PAPER

View Article Online
View Journal | View Issue

Cite this: *RSC Adv.*, 2025, **15**, 34960

Electrochemical behavior and biocompatibility of TiO_2@C core–shell NWs deposited by PECVD for cellular interface application

Roaa Sait, *[a] Raghad Alzahrani,[a] Nabeel Aslam,[b] Shofarul Wustoni, [c] Camelia Florica, [b] Andrea Diaz-Gaxiola, [d] Georgian Melinte,[b] Yaping Zhang, [b] Youyou Yuan, [b] Mohammed Nejib Hedhili, [b] Sridhar Govindarajan, [e] Ahad Syed,[b] Imed Eddine-Gallouzi, [d] Sahika Inal [c] and Hala Aljawhari [a]

The selection of materials for neural interface electrodes relies heavily on two key criteria: electrochemical performance and biocompatibility. Carbon-based nanomaterials have attracted significant attention in neural interface research due to their excellent electrical conductivity, biocompatibility, and mechanical stability. However, achieving desirable electrochemical properties typically requires high-temperature synthesis (>1000 °C), which limits their integration with temperature-sensitive substrates and restricts broader device compatibility. In this study, we investigate TiO_2@C core–shell nanowires (NWs) synthesized at a low temperature of 320 °C *via* plasma-enhanced chemical vapor deposition (PECVD), followed by *in situ* annealing at 450 °C, 550 °C, and 650 °C for durations of 1, 3, and 5 hours. We systematically evaluated their charge storage capacity, electrochemical impedance, long-term cycling stability, and *in vitro* biocompatibility. The 5 nm carbon shell, *in situ* annealed at 650 °C for 3 hours, demonstrated the highest areal capacitance of 874.4 μF cm^{-2} at 50 mV s^{-1} and a low impedance of 2.1 kΩ at 1 kHz, with 92% capacitance retention after 1000 cyclic voltammetry (CV) cycles. In addition, the electrode maintained stable performance across a range of scan rates, indicating resilience under dynamic stimulation conditions. Initial cell culture assays using HeLa cells confirmed the coating's cytocompatibility, supporting viable and non-cytotoxic cellular activity comparable to conventional substrates. These results highlight the potential of moderate-temperature synthesized TiO_2@C core–shell nanowires as high-performance, biocompatible electrode materials with improved compatibility for integration into diverse neural interface platforms.

Received 28th July 2025
Accepted 15th September 2025

DOI: 10.1039/d5ra05460e

rsc.li/rsc-advances

1 Introduction

Neural electrode devices have become essential tools for health monitoring, offering high sensitivity and specificity in detecting, stimulating, and modulating biological signals by establishing a direct interface with nervous tissue. They are crucial in a range of applications, including neuroprosthetics, such as cochlear implants; brain-computer interfaces, which allow individuals with paralysis to control external devices like robotic arms or computer cursors using neural signals; and the treatment of neurological disorders, such as deep brain stimulation used in managing Parkinson's disease and epilepsy.[1] Additionally, these devices are increasingly employed in the rehabilitation of injured soldiers, where targeted neurostimulation has shown promise in enhancing motor function, accelerating recovery, and improving cognitive performance following trauma.[2] Recent progress in neural electrode technologies has concentrated on improving their performance by utilizing advanced materials, adopting innovative fabrication methods, and implementing novel electrode designs. An optimal interface material must demonstrate outstanding biocompatibility, mechanical robustness, low impedance, sufficient charge storage capacity (CSC), and long-term stability to ensure effective communication between the device and neural tissue. Furthermore, the fabrication processes should be scalable, avoiding excessive complexity or prohibitive costs, and must not rely on high-temperature synthesis methods that could hinder compatibility with temperature-sensitive substrates and limit integration with advanced bioelectronic platforms.

[a]*Faculty of Science, Department of Physics, King Abdulaziz University, Jeddah 21589, Saudi Arabia. E-mail: sait.roaa@gmail.com; Tel: +966 12 263-289*

[b]*Core Laboratories, King Abdullah University of Science and Engineering, Thuwal 23955-6900, Saudi Arabia*

[c]*Organic Bioelectronics Laboratory, Biological Science and Engineering Division, King Abdullah University of Science and Engineering, Thuwal 23955-6900, Saudi Arabia*

[d]*Bioscience Laboratory, Biological and Environmental Sciences and Engineering, King Abdullah University of Science and Engineering, Thuwal 23955-6900, Saudi Arabia*

[e]*Emerging Technologies Research Centre, De Montfort University, The Gateway, Leic ester, LE19BH, UK*

With all these challenges, the need to decrease the size of neural electrode devices, to increase selectivity and reduce inflammatory response and scar tissue, makes it even more challenging to find an optimum interface material. Therefore, over the past years, various materials and structures have been employed to enhance the performance of the interface materials, with nanostructure-coated electrodes receiving the most attention.[3] It was found that nanostructure materials enhanced electrochemical performance, which was attributed to their increased surface area, facilitating better charge transfer. For example, a large impedance reduction of approximately 6-times has been reported in gold-nanowires (Au-NWs) electrode as compared to the Au-Flat electrode (4.6 kΩ and 30.3 kΩ at 1 Hz, respectively).[4] Similarly, Boehler *et al.* reported that a grass-like Pt layer resulted in a 60-fold decrease in impedance compared to a smooth Pt electrode.[5] Furthermore, vertical NWs arrays have also shown an enhancement in neural cell adhesion, and a study done by Ana Bajo *et al.* showed that Ni-based nanostructured electrodes increase cell survival, boost neuronal differentiation, and reduce glial cells with respect to flat counterparts.[6]

Carbon nanomaterials have also become integral to the advancement of neural interfaces. The carbon material allotropes, such as carbon nanotubes (CNTs),[7,8] graphene,[9] glassy carbon (GC),[10,11] and modified diamond[12] layer, have all been investigated for neural electrode interface applications. Each form has unique properties suitable for different aspects of neural interfacing. In fact, for example, GC demonstrated superior electrochemical stability and durability compared to Pt electrodes, maintaining functionality over 5 million stimulation pulses with minimal impedance change and adequate charge transfer capacity.[10] Similarly, CNT modified on gold microelectrode arrays (Au-MEAs) significantly reduced electrode impedance by 50% at 1 kHz compared to unmodified Au-MEAs, demonstrating the advantages of nanoscale carbon integration for neural signaling.[7] Post-treatment of diamond surfaces has also been shown to significantly enhance areal capacitance, from 17 μF cm^{-2} in untreated diamond to 1070 μF cm^{-2}, demonstrating the tunability of carbon-based materials.[12] However, the synthesis of these carbon nanostructures often requires high temperatures of around 800–1400 °C for methods like CVD or pyrolysis, which restricts compatibility with temperature-sensitive materials, increases fabrication complexity and cost, hinders scalability, and may compromise biofunctionality or cause mechanical stress in multi-material systems.[13] Consequently, many studies have turned to alternative methods, such as transferring pre-grown graphene sheets onto substrates, though this manual process raises concerns regarding reliability, as consistent adhesion and durability can be challenging to maintain.[14] To address these limitations, advancements in low-temperature and template-assisted fabrication processes are being explored. Template-assessed process can serve as a substrate for depositing other materials allowing for controlled synthesis. Among these templates, anodic metal oxide materials, such as titania (TiO_2), are particularly effective for creating high-aspect-ratio, ordered nanostructures with large surface areas, all achievable within the desired low-temperature range. Titania is also recognized for its outstanding biocompatibility and corrosion resistance, making it ideal for biomedical applications. Huang *et al.* demonstrated the use of TiO_2 nanotubes as a template for IrO_2 deposition, synthesizing a TiO_2@IrO_2 core–shell structure, with the IrO_2 layer having a thickness of 18 nm.[15] This configuration enhanced CSC from 5.04 to 42.84 mC cm^{-2} compared to a planar design and demonstrated stable cyclability over 1000 CV cycles.[15]

In this work, we introduce a low-temperature PECVD method to coat TiO_2 nanowires with a conformal carbon shell at 320 °C followed by *in situ* annealing in argon at moderate temperatures of 450, 550, and 650 °C for 1, 3, and 5 hours. We then systematically assess how these moderate post-treatments conditions influence the material's structure, electrochemical behavior, and biocompatibility for cellular-interface applications. Although TiO_2@C core–shell structures have been previously synthesized for lithium-ion batteries,[16,17] photocatalysis,[18] and fuel cell applications,[19] to the best of our knowledge, they have not yet been investigated for cellular interface applications. By tuning the annealing temperature and duration, we identify the optimal balance between carbon shell integrity and electrochemical performance, achieving high capacitance and low impedance without resorting to high temperatures or prolonged processing. Our approach not only reduces the overall thermal budget but also provides precise control over shell properties, making these TiO_2@C nanowires especially promising for integration into biocompatible electrode platforms and systems that require compatibility with temperature-sensitive materials.

2 Experimental

2.1 TiO_2@C-NWs preparation

As illustrated in Fig. 1, TiO_2-NWs were synthesized on FTO/glass substrates using the hydrothermal method according to a previously reported method.[20] The growth solution was prepared by mixing 1 ml of titanium butoxide (TNB, 98+%, Strem Chemicals, Inc), 30 ml of hydrochloric acid (HCl, 37 wt%, ACS reagent, Sigma-Aldrich), and 30 ml of deionized water (DI). This mixture was sonicated for 10 minutes until a clear solution was formed. Subsequently, 12 ml of the resulting solution was transferred into a 25 ml Teflon-lined autoclave, where FTO/glass substrates were placed at an inclined angle against the Teflon wall, with the conductive surface facing downward. The autoclave was sealed and placed in a furnace (Binder) for the hydrothermal reaction, which was conducted at 150 °C for 5 hours. After the hydrothermal growth, the autoclave was cooled by placing it under running water. Once cooled, the samples were carefully extracted and thoroughly rinsed multiple times with deionized water to remove any residual precursors. Finally, the substrates were blow-dried using nitrogen gas. This process yielded a uniform, white coating of TiO_2-NWs across the entire substrate surface, as seen in Fig. 1.

For carbon deposition, Radio Frequency (RF)-PECVD system (Oxford Plasma Lab 100; 13.56 MHz) tool was used. A controlled gas mixture of CH_4 and Ar in a 1 : 2.5 ratio was employed as the

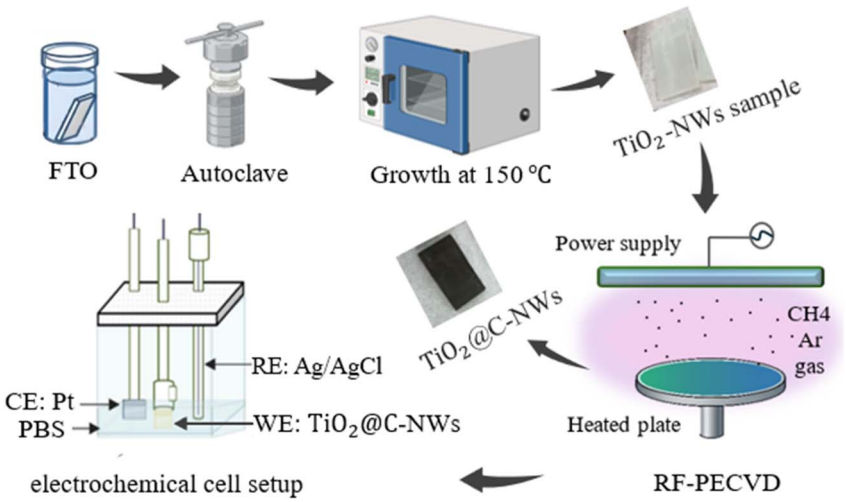

Fig. 1 Schematic illustration of the synthesis process of TiO_2@C core–shell NWs, followed by electrochemical characterization using a three-electrode cell setup.

precursor for carbon film growth. The samples were mounted onto the anodic electrode stage (8-inch diameter). Initially, the chamber was evacuated to a base pressure of approximately 2.7 $\times$ 10^{-6} torr. The substrate temperature was then gradually raised to 320 °C. Upon reaching the target temperature, CH_4 and Ar were introduced into the chamber at flow rates of 200 sccm and 500 sccm, respectively, controlled *via* mass flow controllers. Plasma was ignited by applying an RF power of 300 W, and the deposition pressure was maintained at 1 torr throughout the process. Carbon deposition on all TiO_2-NWs samples was conducted for one hour under these conditions. Upon completion of carbon deposition, the RF power was switched off, and the chamber was purged with Ar gas only.

The *in situ* annealing process then commenced immediately after the carbon deposit, without removing the samples from the PECVD chamber. This approach was chosen to minimize contamination and oxygen exposure. The chamber was filled with Ar gas, and the substrate temperature was gradually increased to the desired value, and for the intended duration. After annealing, the samples were allowed to cool to room temperature under continuous argon flow. A visible color change in the samples from white to dark gray, as seen in Fig. 1, indicated successful carbon coating. For clarity and consistency, each TiO_2@C-NW sample is labeled according to its *in situ* annealing temperature (in °C) followed by the duration (in hours).

2.2 Physicochemical characterizations

The *in situ* annealed TiO_2@C-NWs samples were analyzed by scanning electron microscopy (SEM), using a Helios 5UX Thermo Fisher Scientific™ instrument to reveal their morphology. The imaging was conducted with a 5 kV acceleration voltage, a 25 pA electron beam current, in immersion mode, with the Elstar in-lens secondary electrons detector (TLD-SE) and employing the interlacing scanning mode with frame integration.

Electron-energy loss spectroscopy (EELS) measurements were performed using a Themis Z microscope from Thermo Fisher Scientific™. The sample preparation involved scraping the grown nanowires from the glass substrate with flat-tip tweezers and placing them into a vial filled with high-purity ethanol. These vials were then ultrasonicated at 800 W and 45 kHz for 1 hour using an Elma Ultrasonic bath to disperse the nanowires evenly throughout the solutions. Finally, 10 microliters of the solution were drop cast onto a Quantifoil 200 mesh copper TEM grid. Prior to the insertion into the microscope, the TEM grid was treated for 7 s in a 5% O_2 plasma to remove residual surface contamination. The microscope was operated at 300 kV acceleration voltage in scanning transmission mode (STEM) with a 21 mrad convergence angle. STEM imaging was performed using a high-angle annular dark field (HAADF) detector with an inner angle of 50 mrad. The STEM EELS spectrum imaging (SI) used in elemental mapping was performed with a Gatan™ Continuum GIF operated at 37 mm camera length and a 5 mm spectrometer entrance aperture. The SI acquisition was performed in Dual mode with a spectrometer dispersion of 0.3 eV per channel, 200 pA beam current, a pixel dwell time of 250 ms and a pixel size of 2 nm. Gatan™ Digital Micrograph software was used for data processing.

XRD (Bruker D8 discover system with a 2D Eiger detector) was used to study the crystallographic orientation of the TiO_2@C-annealed samples. A Cu Kα X-ray radiation source having a characteristic wavelength of 1.5418 Å was used. The XRD pattern in the 2θ range was recorded from 20 to 80° with a step size of 0.02° and a time per step of 0.5 s.

Raman spectroscopy measurements were carried out using a WiTec Apyron Confocal Raman Spectrometer (Oxford Instruments) at room temperature. The excitation source was a DPSS 532 nm laser with a power of 20 mW set by the control software. Scattered light from the sample surface was coupled into an ultra-high throughput spectrometer *via* 300 grooves per mm grating and detected by a highly efficient thermoelectrically cooled spectroscopy camera. A Zeiss Epiplan–Neofluar 50x/0.55

long working distance objective was applied for all measurements. The laser spot size on the sample surface was approximately 1.2 μm, and the spectral resolution was around 4 cm^{-1}. The D and G carbon bands were fitted by Lorenze peak functions using the advanced fitting tool provided by WITec data analysis software. The ratio of I_G/I_D was calculated based on the fitting results.

The XPS measurements were carried out in a Kratos Axis Supra spectrometer ($h\nu = 1486.6$ eV) operating at 75 W, a multichannel plate, and a delay line detector under a vacuum of 1×10^{-8} mbar equipped with a monochromatic Al Kα X-ray source. Survey and high-resolution spectra were performed at fixed analyzer pass energies of 160 and 20 eV, respectively. Samples were mounted in the floating mode to avoid differential charging. Charge neutralization was required for all samples. Binding energies were referenced to Ti $2p_{3/2}$ from TiO_2 set at 458.8 eV binding energy. Survey spectra, as well as high-resolution spectra of Ti 2p, C 1s, and O 1s core levels, were recorded.

2.3 Electrochemical characterization

The electrochemical performances of *in situ* annealed TiO_2@C-NWs samples were evaluated through cyclic voltammetry (CV) and electrochemical impedance spectroscopy (EIS) measurements with a three-electrode configuration using a potentiostat (VSP-300, BioLogic Instrument), as illustrated in Fig. 1. A platinum (Pt) wire was used as the counter electrode, and an Ag/AgCl electrode (in 3 M KCl) was used as the reference electrode. The working electrode area was set to 1 cm^2 for all measured samples to facilitate convenient calculation of current density. To achieve this, epoxy resin was applied to the electrode surface, exposing only 1 cm^2. The electrolyte was a 10 mM PBS solution (pH 7.4), chosen to mimic the physiological buffer conditions of the human body. All samples were scanned within a potential range of −0.2 to +0.8 V at a rate of 50 mV s^{-1}. This 1 V scan window was chosen after testing wider ranges, which indicated a risk of electrolysis at higher potentials. For the electrochemical stability test, a scan rate of 100 mV s^{-1} was applied for 1000 cycles. Impedance measurements were conducted every 200 cycles after allowing the electrode to stabilize at open circuit potential (OCP) for 15 minutes. During each impedance measurement, a 10 mV sinusoidal perturbation was applied at the OCP across a frequency range of 100 kHz to 1 Hz. All measurements were conducted at room temperature inside a grounded Faraday cage to prevent external electromagnetic interference from affecting the accuracy of the measurements. The areal (C_a) capacitance was calculated using the following equation:

$$C_a = \frac{i}{s \cdot v} = \frac{\left(\int_{V_a}^{V_c} i(v)\ \mathrm{d}v\right) \Big/ (V_c - V_a)}{s \cdot v} \quad (1)$$

where i is the current, which can be obtained by integrating the area of the CV curves from the upper voltage limit (V_c) to the lower voltage limit (V_a), s is the surface area of the electrode material exposed to the electrolyte (cm^2), and v denotes the potential sweep rate (mV s^{-1}).[21]

2.4 Cell culture preparation and analysis

For the cellular interface experiment, TiO_2@C-NWs and TiO_2@C-film substrate (2 cm × 1 cm) treated at 550 °C for 3 hours were chosen and prepared for cell culture. Control samples consisted of standard 35 mm μ-dishes (ibidi, cat. no. 81156) serves as tissue culture-treated plastic references. The sample substrates used for cell adhesion and viability assessments were sterilized by autoclaving at 121 °C and 1 atm for 20 minutes to ensure complete decontamination. The sample substrates were carefully positioned in the center of individual wells in ultra-low attachment 6-well plates (corning, cat. no. 3471). HeLa human epithelial cell lines (Sigma-Aldrich, cat. no. 93021013) were cultured as sub-confluent monolayers in Dulbecco's Modified Eagle Medium/Nutrient Mixture F-12 (DMEM/F12, Gibco), supplemented with 10% fetal bovine serum (HI-FBS, Gibco) and 1% penicillin–streptomycin (Gibco). Cells were maintained in a humidified incubator at 37 °C under 5% CO_2 atmosphere. Cytotoxicity testing was conducted using a direct contact method following with ISO 10993-5 (or EN 30993-5).[22]

A homogeneous cell suspension with a concentration of 2.6×10^5 cells per mL was prepared. For initial seeding, 200 μL of this suspension was gently pipetted directly onto the surface of each test sample to ensure uniform coverage and direct contact. After a 2-hour pre-incubation to allow cell adhesion, 3 mL of fresh culture medium was added to each well to submerge the samples and support further cell growth. At 24 hours post-seeding, cells were enzymatically detached using TrypLE™ Express (Gibco), collected by centrifugation, and resuspended in 200 μL of media. Cell proliferation was quantified using an automated hemocytometer (Countess 3, Thermo Fisher Scientific).

For the viability assay, cells were cultured under the same conditions as above but were allowed to remain on the substrates for imaging. Live/dead staining was performed using the Live/Dead® Viability/Cytotoxicity Kit (Thermo Fisher Scientific, cat. no. L3224), which uses calcein AM and ethidium homodimer-1 to distinguish live (green) and dead (red) cells, respectively. To ensure optimal imaging, each sample was carefully inverted within its well to expose the cell-covered surface toward the objective lens, then imaged using a fluorescence inverted microscope (EVOS M500, Thermo Fisher Scientific).

Quantification of live and dead cells was conducted by analyzing the acquired fluorescence images using Fiji (ImageJ) software. Cell viability and proliferation experiments were performed using three different cell passages (P10, P14, and P21), and each experimental condition was tested in triplicate to ensure statistical reliability and reproducibility.

3 Results and discussion

3.1 SEM and STEM-EELS analysis

Fig. 2(a–d) presents SEM images of pristine TiO_2-NWs grown on FTO/glass substrate, while Fig. 2(e–h) presents SEM images of the TiO_2-NWs after carbon deposit (650 °C–3 h). Images taken at

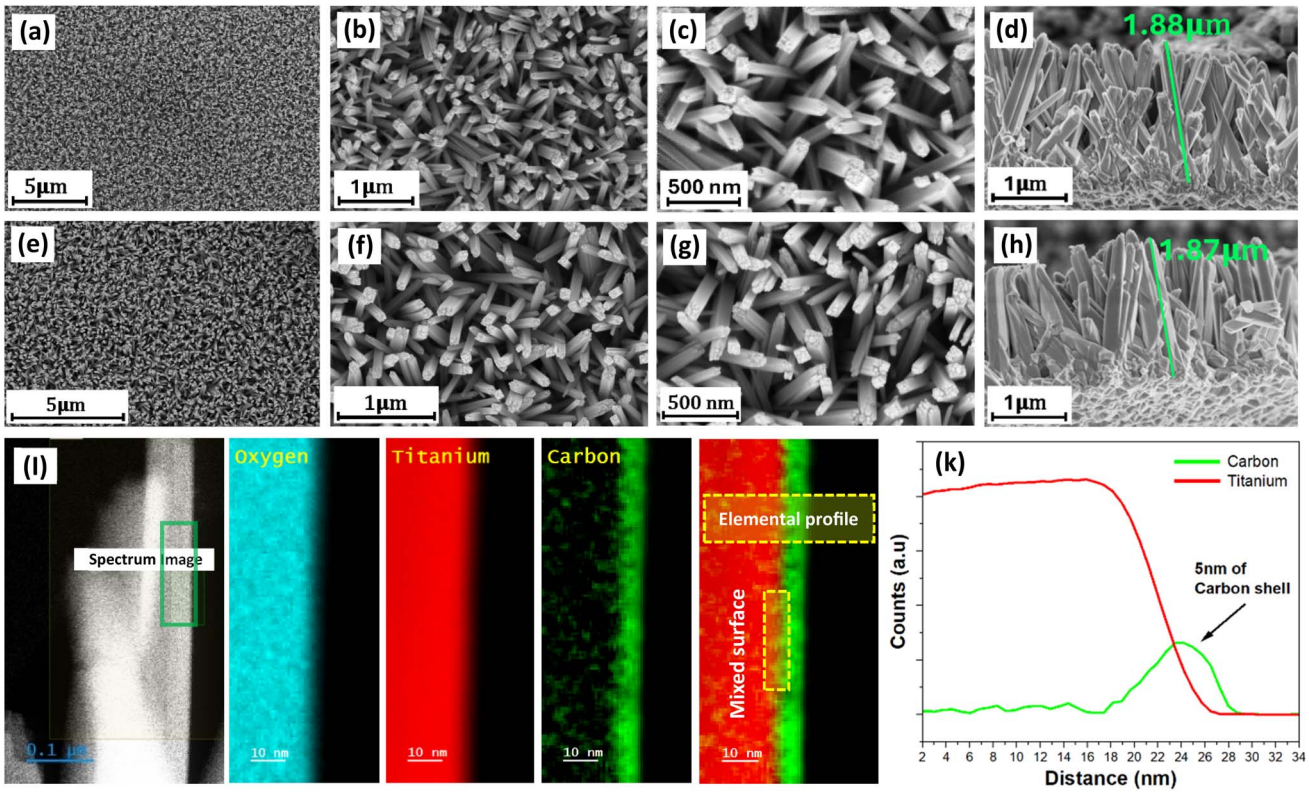

Fig. 2 SEM images of (a–d) pristine TiO_2-NWs, (e–h) TiO_2@C core–shell NWs annealed at 650 °C for 3 hours, (i) its STEM image and EELS elemental mapping, and (k) Elemental profile for C and Ti-edge.

various locations and magnifications confirm that the TiO_2-NWs uniformly cover the substrate, with most nanowires oriented perpendicularly to the surface. The NWs display a well-defined tetragonal shape with square top faces, an average diameter of approximately ~160 nm, and a length of ~1.9 μm. The top surfaces feature distinct step edges, providing some degree of roughness, while the side surfaces appear relatively smooth. With carbon deposition and subsequent *in situ* annealing at different temperatures and durations, the morphology and aspect ratio of TiO_2-NWs remained unchanged across all samples. To investigate the structural properties and thickness of the carbon shell, STEM-EELS was conducted. Fig. 2(i) and (k) present the elemental maps and profile of the 650 °C–3 h sample, showing distinct spatial distributions of Ti, O, C, and composite EELS maps that overlay Ti and C. It can be seen that the carbon homogenously encases the nanowire, confirming the TiO_2@C core–shell structure. A line profile extracted from the region indicated by the dashed box quantitatively verifies a carbon shell thickness of approximately 5 nm, as shown in Fig. 2(k). Additional EELS measurements including the as-deposited carbon layer at 320 °C and other *in situ*-annealed samples under different temperatures and durations, Fig. S1 (SI), further corroborate the uniformity of the carbon coating, and confirms that the shell thickness remained unchanged across these conditions, indicating that the annealing process did not lead to carbon layer degradation. While some studies have reported a reduction in carbon layer thickness at annealing temperatures above 400 °C, attributed to densification, carbon desorption, or adhesion loss,[23,24] others have shown that amorphous carbon remains thermally stable when deposited onto metals or transition metal nitrides substrates.[25] Our findings align with the latter, demonstrating that the TiO_2 surface effectively stabilizes the carbon shell during high-temperature annealing, preventing delamination.

To further characterize the chemical bonding nature of TiO_2@C-NWs structure and evaluate the effect of varying *in situ* annealing, high-energy-loss EELS spectra were acquired for the 450 °C–3 h, 550 °C–3 h, and 650 °C–3 h samples, along with the as-deposited carbon. These spectra, recorded in the range of 270–600 eV from the TiO_2–carbon interface region, are presented in Fig. 3(a). The spectra reveal the C–K, Ti–L, and O–K edges, allowing simultaneous insight into both the carbon shell and the underlying oxide core. For the carbon feature, the peak at ~285 eV corresponds to the C 1s–π* transition, which is characteristic of sp^2-bonded carbon (C=C) and is typically associated with graphitic structures.[26] The broader feature around ~290 eV aligns with the C 1s–σ* transition, indicative of sp^3 diamond-like carbon bonds.[26] The observed broadening and smoothing of the σ* peak suggest the presence of both sp^2 and sp^3 bonding within the carbon shell, consistent with an amorphous carbon structure (a-C). Comparison between the as-deposited and *in situ* annealed samples indicates that annealing induces no substantial alteration in the bonding configuration of the carbon layer, which remains predominantly amorphous. However, closer examination of the normalized C–K edge spectra reveals minor variations in peak intensity,

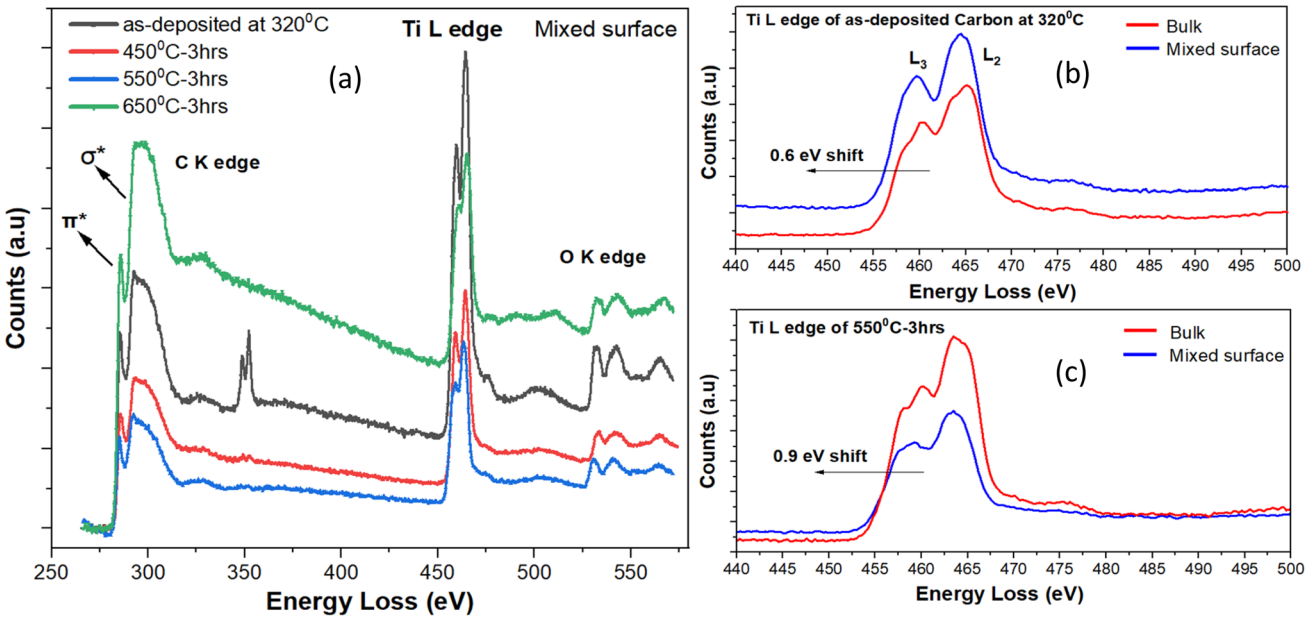

Fig. 3 (a) Overall EELS spectrum (from TiO_2–C interface) of as-deposited TiO_2@C core–shell NWs and *in situ* annealed at 450 °C, 550 °C, and 650 °C for 3 hours, (b) Ti L-edge of the as-deposited TiO_2@C core–shell NW and (c) the *in situ* annealed at 550 °C for 3 hours.

particularly in the sample annealed at 650 °C–3 h, which may reflect subtle structural reordering or slight changes of the sp^2/sp^3 ratio. In this context, both the 550 °C and 650 °C annealed samples exhibit an increase in graphitized features, evidenced by the enhanced π* peak and a more distinct structure in the broad σ* region, implying a gradual enrichment in sp^2 bonding with increased annealing temperature. Notably, the sample annealed at 650 °C for 5 hours (as highlighted in the inset of Fig. S2) also exhibits a pronounced intensity in both sp^2 and sp^3 features, indicating a possible peak in structural changes at this condition; however, quantifying the sp^2/sp^3 ratio *via* EELS could be a challenge due to the different orientation of the nanowire relative to the incident electron beam which can introduce anisotropic scattering effects. Moreover, the changes in the sp^2/sp^3 ratio are often too small to quantitatively resolve them, further affecting the interpretation of the data.

Another notable effect of annealing, observed by examining the Ti L-edge at the TiO_2–carbon interface compared to the bulk (Fig. 3(b and c)), is a 0.6 eV chemical shift toward lower energy in the as-deposited sample. This shift indicates a partial reduction of Ti^{4+} to Ti^{3+} at the interface, while the bulk remains fully oxidized. Upon annealing at 550 °C for 3 hours, the shift increases to approximately 0.9 eV (Fig. 3(c)), suggesting enhanced interfacial reduction or a higher concentration of Ti^{3+} species. MLLS fitting of the 650 °C–3 h sample further confirms this trend, revealing clear spatial co-localization of Ti^{3+} with carbon, unlike the as-deposited sample, where no such correlation is observed, see Fig. S3. This tandem distribution implies that high-temperature annealing facilitates localized reduction of Ti^{4+} in the presence of carbon. Additionally, EELS mapping shows a high density of microstructural defects, such as cracks and voids, in both samples. Notably, in the 650 °C–3 h sample, Ti^{3+} species extend beyond surface facets into these defect-rich regions, indicating that such defects may act as active sites for reduction or diffusion pathways.

3.2 Raman spectroscopy analysis

Raman spectroscopy is a powerful technique for assessing the structural characteristics of graphitic carbon materials. In such materials, the prominent features are the G band, typically centered around ~1580 cm^{-1}, and the D band, near ~1360 cm^{-1}. The G band originates from the first-order scattering of the E_2g phonon mode, corresponding to the in-plane stretching vibrations of sp^2-hybridized C–C bonds within well-ordered graphitic domains.[27] In contrast, the D band is associated with A_{1g} mode symmetry, linked to structural disorder and defects in the carbon layer, such as edges, vacancies, or other imperfections, and is often attributed to sp^3-hybridized carbon.[27] The degree of graphitization is quantitatively evaluated by the intensity ratio of the G to D bands (I_G/I_D), as well as their full width at half-maximum (FWHM) and the band position. A higher I_G/I_D ratio reflects a greater extent of graphitic ordering, while a narrower FWHM shows unstrained or defect-free sp^2 clusters.

Fig. 4(a) presents the Raman spectra of the as-deposited TiO_2@C-NWs and those subjected to *in situ* annealing at various temperatures for an annealing duration of 3 hours. These samples were selected as representative midpoints in the annealing duration to capture the general structural evolution. Each spectrum is the average of five measurements taken at different regions across each sample to ensure spatial consistency and reduce local variation effects. It can be seen that the Raman spectra picks up the strong Ti–O peaks corresponding to that of TiO_2-NWs which are in the rutile phase, evidenced by the presence of three characteristic Raman-active modes of rutile;

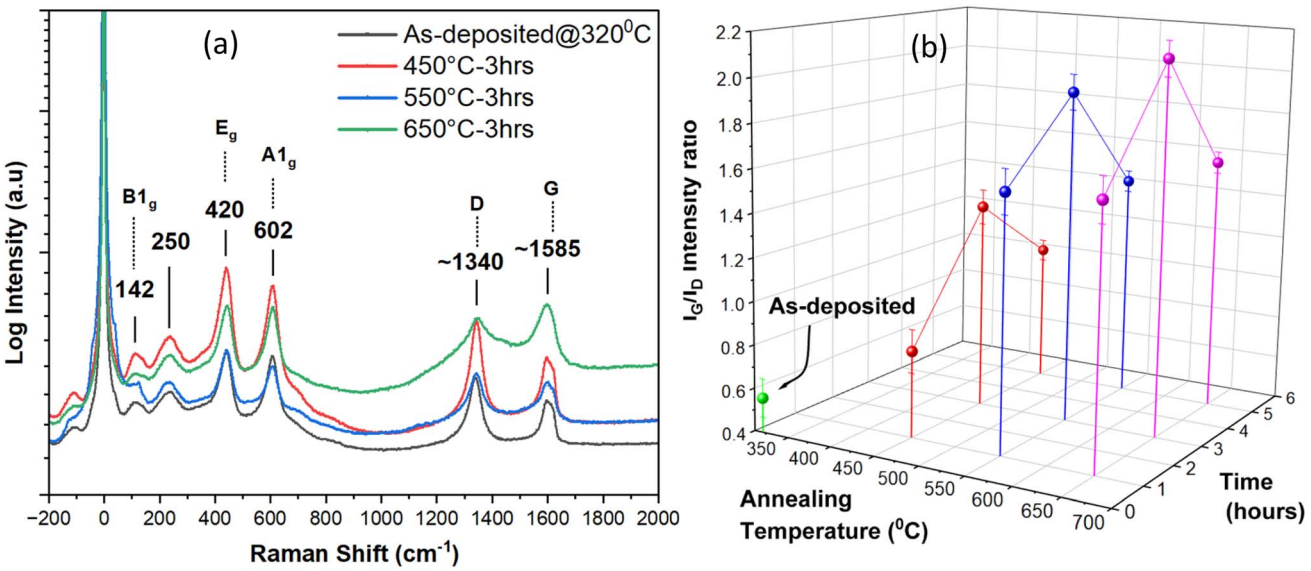

Fig. 4 (a) Raman spectroscopy of as-deposited TiO_2@C core–shell NWs and *in situ* annealed at 450 °C, 550 °C, and 650 °C for 3 hours, (b) I_G/I_D ratio of all treated samples.

$B1_g$, E_g, and $A1_g$, observed at 142, 420, and 602 cm^{-1}, respectively.[28] The $A1_g$ and $B1_g$ modes arise due to the antisymmetric and symmetric bending vibration of O–Ti–O, respectively, while the E_g mode is due to the O–Ti–O symmetric stretching vibration in TiO_2.[28] Additionally, a broad band at 250 cm^{-1} is present, which has been reported to be attributed to multiple phonons scattering due to the disordered lattice of NWs structure, as noted by Ma *et al.*[29] Notably, this rutile phase remains stable across varying annealing temperatures, as further confirmed by the XRD analysis presented in Fig. S4, emphasizing the phase stability of the synthesized nanowires. The Raman spectrum of pristine TiO_2-NWs clearly shows no carbon-related peaks (Fig. S5), and after carbon deposition, all samples subjected to varying *in situ* annealing conditions exhibit two peaks at 1340 and 1585 cm^{-1}, corresponding to the D and G bands of carbon,[27] respectively. The intensity ratio of the G-band to the D-band (I_G/I_D) of all treated samples was calculated and is displayed in Fig. 4(b). It can be seen that the I_G/I_D ratio evolves significantly with annealing temperature and duration from ~0.8 to a maximum of ~2. The as-deposited sample shows a low I_G/I_D ratio (0.6), indicating a high level of disorder and a dominant sp^3 character in the carbon matrix. Upon annealing at higher temperatures, the I_G/I_D ratio increases, peaking at 650 °C after 3 hours of annealing. This trend suggests a notable transformation from disordered to more graphitic (sp^2-rich) structures, likely due to thermal activation enabling atomic rearrangement and partial healing of defects. Similar trends have been reported for carbon deposited at various temperatures, where I_G/I_D ratio increased when temperature increased from 400 to 700 °C, indicating enhanced graphitization.[30,31] However, with prolonged annealing beyond 3 hours, the I_G/I_D ratio appears to decline slightly, possibly due to reintroduced disorder or limitations imposed by the carbon layer's ultrathin 5 nm thickness, which could constrain the growth of graphitic domains or cause structural instability at elevated temperatures.[32]

The bands positions and their FWHM were also seen to change with the annealing process, as shown in Table 1. Here the G-band exhibits a consistent red shift, decreasing from 1603.6 cm^{-1} in the as-deposited state to 1579.9 cm^{-1} at 650 °C for annealing duration of 3 hours. Conversely, the D-band shows a blue shift, increasing from 1337.7 cm^{-1} in the as-deposited state to approximately 1367.1 cm^{-1} under the same annealing conditions. This shift may also reflect the evolution of sp^2 cluster structures, where smaller or different-sized clusters become more prominent.[33,34] Such trends are consistent with previous studies that associate D-band blue shifts and G-band red shifts with a thermally induced evolution in the distribution and size of sp^2 clusters.[35] However, the FWHM of both the D and G bands increases with temperature. This broadening is often associated with increased structural disorder, such as variations in bond lengths and bond angles within and between sp^2 domains. It suggests that even as cluster size may increase, disorder in the local bonding environment becomes more significant, contributing to the broader spectral features.[34] These observations confirm the tunability of the

Table 1 Raman shifts for D and G bands

	D-band		G-band	
Samples	Position (cm^{-1})	FWHM	Position (cm^{-1})	FWHM
As-deposited@320 °C	1337.7	41.5	1601.6	34.6
450 °C–3 h	1341.7	37.2	1594.8	37.3
550 °C–3 h	1341.2	39.5	1598.6	38.9
650 °C–3 h	1367.1	57.1	1579.9	43.1

carbon film's bonding configuration and defect density through controlled annealing processes, which is critical for optimizing its performance in neural interface application.

3.3 X-ray photoelectron spectroscopy analysis

To gain deeper insight into the surface elemental composition and carbon bonding states, XPS analysis was conducted on the as-deposited TiO_2@C-NWs and *in situ* annealed samples at 450 °C, 550 °C, and 650 °C for annealing duration of 3 hours. The survey spectra (shown in Fig. S6) confirm the presence of C 1s, O 1s, and Ti peaks, along with minor nitrogen contamination from the atmosphere, with no other detectable elements. The high-resolution core-level spectra for C 1s and Ti 2p are shown in Fig. 5(a and b), respectively. The C 1s spectra display a dominant peak around 284.5 eV, corresponding to the sp^2/sp^3-hybridized carbon network.[36] Additional lower-intensity peaks at approximately 286.4 eV and 288.6 eV are assigned to carbon–oxygen species such as C–O and C═O bonds, consistent with surface oxidation.[36]

Comparison of the C 1s spectra across all annealed samples (450 °C, 550 °C, and 650 °C) reveals minimal variation in spectral shape, indicating that the sp^2/sp^3 carbon ratio remains largely unchanged with increasing annealing temperature. This observation contrasts with the Raman spectroscopy results, which showed a clear evolution in graphitization. This difference likely arises because XPS probes only the surface a few nanometers and is sensitive to surface oxidation and contamination, which can mask subtle changes. Meanwhile, Raman probes deeper into the bulk and is more sensitive to sp^2 clustering and ordering, capturing structural changes that are not reflected in the surface-sensitive XPS data. Additionally, the C 1s spectrum reveals the presence of TiC, identified by a characteristic peak at lower binding energy around 281.5 eV, which emerges in the treated samples as well as the as-deposited sample. This observation is supported by the Ti 2p spectra, which show signals between 455 eV and 458 eV corresponding to Ti^{2+} and Ti^{3+} oxidation states. The presence of these reduced titanium species aligns well with the EELS analysis, which confirmed the existence of Ti^3.

3.4 Electrochemical characterization through CV & EIS

3.4.1 Cyclic voltammetry (CV). Fig. 6(a) displays the CV curves of TiO_2@C-NWs *in situ* annealed at 450 °C, 550 °C and 650 °C for 1, 3, and 5 hours, while Fig. 6(b) summarizes the corresponding areal capacitance. All the CV curves were recorded from the 4th cycle to ensure the electrodes had reached a stable electrochemical state in conjunction with the electrolyte solution. It can be seen that the as-deposited carbon exhibits no capacitive behavior, characterized by near-zero current density, indicating that the carbon layer in its as-deposited state is electrochemically inactive, as expected. In contrast, annealing significantly enhances electrochemical activity, with the structures showing clear capacitive characteristics. According to Singh *et al.*,[37] the transformation of the carbon layer from an inactive (insulating state) to an electrochemically active state is primarily due to the structural modifications induced by annealing. The observed variations in CV shapes, and hence areal capacitance across different annealing conditions can be correlated with changes in the carbon's bonding structure, as confirmed by Raman, EELS, and XPS analyses. At an annealing temperature of 450 °C, a modest enhancement in areal capacitance is observed as compared to the as-deposited carbon. The areal capacitance slightly increases from 0.23 to 1.93 μF cm^{-2} as the annealing duration extends from 1 to 5 hours. This improvement may correspond to the slight increase in the sp^2/sp^3 carbon ratio, as evidenced by Raman spectroscopy, and possibly the presence of a small amount of TiC, as indicated by XPS. However, this enhancement in areal capacitance with increasing annealing duration remains limited. In contrast, annealing at 550 °C results in

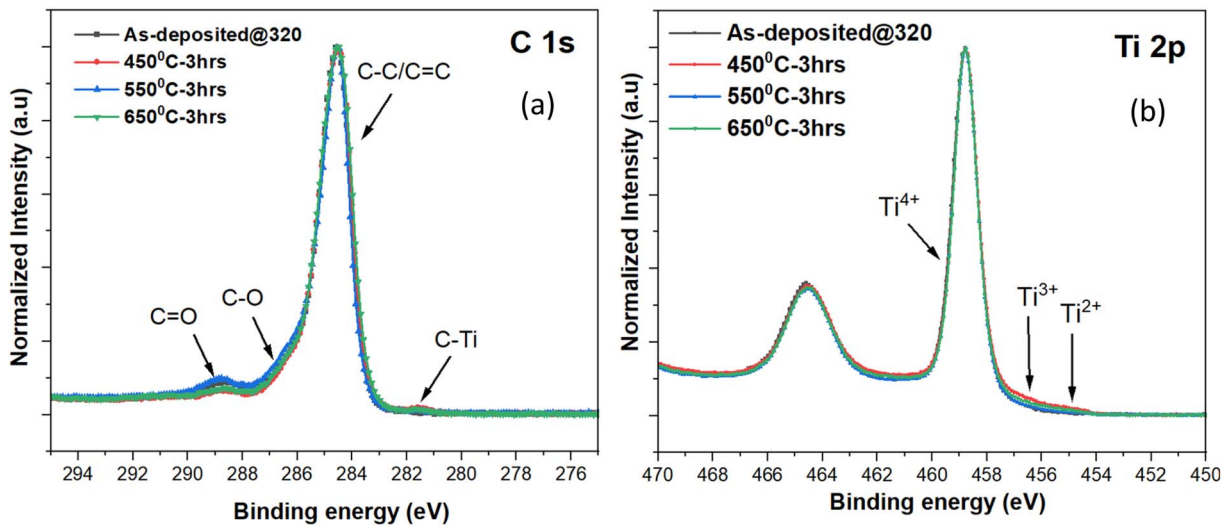

Fig. 5 XPS of as-deposited TiO_2@C core–shell NWs and *in situ* annealed at 450 °C, 550 °C, and 650 °C for 3 hours, showing (a) C 1s core-level, (b) Ti 2p core-level.

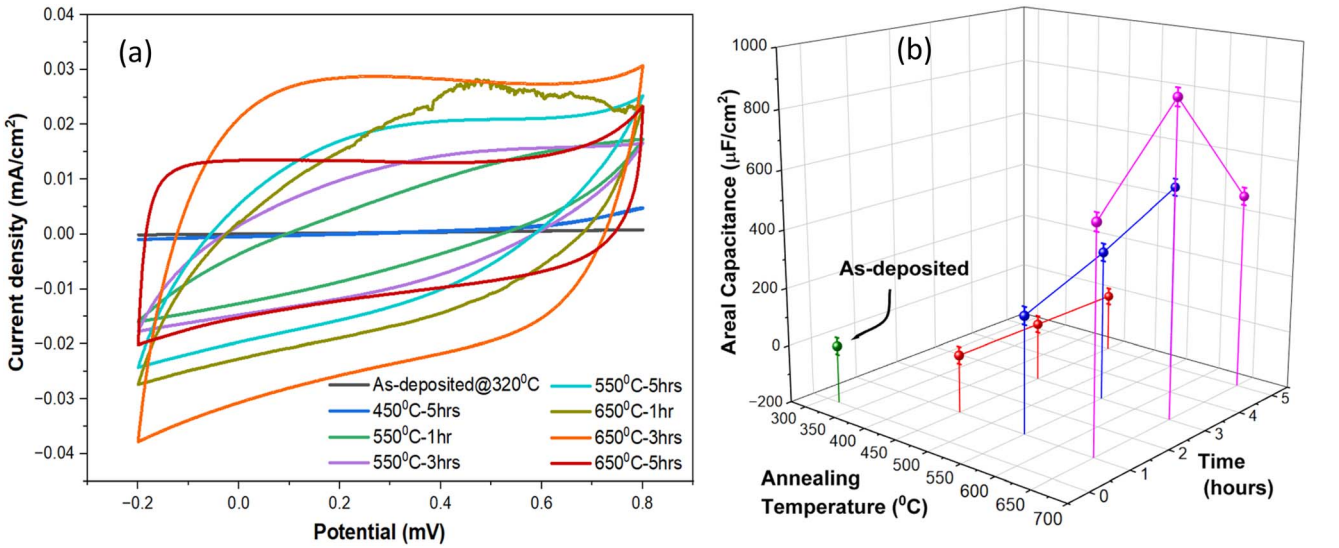

Fig. 6 (a) CV measurements of as-deposited TiO_2@C core–shell NWs and *in situ* annealed at 450 °C, 550 °C, and 650 °C for varying duration showing (b) corresponding areal capacitance.

a significantly more pronounced increase in areal capacitance, from 200.4 to 459.6 μF cm^{-2} over the same duration. This trend aligns with a marked rise in the sp^2/sp^3 carbon ratio from 1.35 to 1.94, which denotes the formation of more conductive graphitic networks. Additionally, EELS analysis at this temperature reveals a relatively higher presence of Ti^{3+} species, inferred from characteristic chemical shifts seen in Fig. 3(c). According to Wang *et al.*, the emergence of Ti^{3+} sites has been shown to increase electronic conductivity and enhance capacitive behavior by introducing localized states and improving charge carrier mobility at the TiO_2 interface, further contributing to the observed capacitance gains.[38] However, the absence of a distinct Ti^{3+}/Ti^{4+} redox couple in the CV suggests that the dominant charge storage mechanism remains electrical double-layer capacitance,[39] possibly with pseudocapacitive contributions. Notably, the CV shape of the samples annealed at 550 °C for different durations exhibits characteristics of a pseudocapacitive response (leaf-like shape), evidenced by a slight distortion of the ideal capacitive rectangular profile.[40] This pseudocapacitance originates from ion accumulation at the electrical double layer, coupled with adsorbed molecules.[40,41]

For further annealing at 650 °C, the areal capacitance reaches a maximum value of 874.4 μF cm^{-2} at 3 hours, which corresponds to the highest sp^2/sp^3 ratio recorded among all annealing conditions (Fig. 4(b)). MLLS fitting of EELS SI data at this condition, revealed a high density of microstructural defects, such as cracks and voids, within the carbon matrix, as well as the distribution of Ti^{3+} species was not just confined to the outer facets of the nanowires but extended into these defect-rich regions (Fig. S3). This spatial delocalization of Ti^{3+} across the defected carbon matrix likely contributed additional charge storage sites, thereby reinforcing the overall electrochemical response at this condition. However, extending the annealing duration at 650 °C to 5 hours results in a noticeable decline in areal capacitance, dropping to 475.8 μF cm^{-2}, becoming comparable to the values observed at 550 °C. This decline is likely attributed to a combination of factors, including a decrease in the sp^2/sp^3 carbon ratio, indicating a shift toward a more sp^3-rich, diamond-like carbon structure that is less conductive. This trend aligns with prior studies that report increased sp^3 bonding at comparable annealing conditions.[42–44] It is plausible that the ~5 nm carbon layer, under extended high-temperature treatment, becomes increasingly crosslinked and structurally hardened, favoring sp^3 hybridization and thus reducing charge transport efficiency.

Interestingly, there is a distinct difference in CV shape between structures annealed at 650 °C for 3 and 5 hours. Structure annealed at 650 °C for 5 hours exhibits more rectangular CV shapes, indicative of dominant electric double-layer capacitive behavior. This suggests that the reduction in microstructural defects leads to reduced adsorbed species, making ion accumulation at the double layer the primary mechanism for charge storage. In contrast, the CV profile of the 650 °C–3 h sample presents a transitional shape between the leaf-like and rectangular profiles. This feature implies the coexistence of both double-layer charging and pseudocapacitive contributions. The enhanced capacitance of 874.4 μF cm^{-2} in this sample can be attributed to both the synergistic effect of extended graphitic ordering and the presence of Ti^{3+} species. These combined mechanisms enable efficient charge storage. Zanin *et al.* deposited a 25 nm diamond-like carbon film onto vertically aligned CNTs by pulsed PECVD at 800 °C, achieving 0.6 mF cm^{-2},[45] while Su *et al.* grew cone-shaped CNT probes *via* thermal CVD (750 °C) with a subsequent 800 °C anneal to report 2.5 mF cm^{-2}.[8] Tong *et al.* synthesized ~200 nm nitrogen-doped ultrananocrystalline diamond films, activated by O_2 plasma and vacuum-annealed above 700 °C, to reach 1.07 mF cm^{-2}.[12] Although these studies demonstrate impressive capacitances, they rely on thicker carbon or diamond layers and higher thermal budgets. These examples confirm that integrating

a crystalline TiO_2 scaffold with an ultrathin carbon shell is a uniquely powerful strategy for pushing areal capacitance into the sub-mF cm^{-2} regime while maintaining a lower annealing temperature and miniaturization potential.

3.4.2 Electrochemical impedance spectroscopy (EIS). Fig. 7(a) presents the Bode plot and phase angle responses of as-deposited TiO_2@C-NWs and *in situ* annealed at 450 °C, 550 °C, and 650 °C for various durations. The plots clearly demonstrate that the impedance behavior is highly sensitive to both annealing temperature and duration, reflecting structural and compositional changes occurring within the carbon shell. The as-deposited sample and the sample annealed at 450 °C for 5 hours both behave almost purely resistively; their impedance magnitude remains high and nearly constant across 10^5–10^{-2} Hz, and the phase angle approaches 0° at low frequencies, clearly demonstrating a poorly conductive carbon layer. In contrast, the samples annealed at 550 °C for 1–5 hours and those annealed at 650 °C for 1 hour exhibit very similar Bode-plot response: in the high-to-mid frequency region the total impedance $|Z|$ is almost independent of frequency (resistive domination), but decreases with higher annealing temperature and duration. Quantitatively, the total impedance $|Z|$ in this region drops from ~23 kΩ after 1 hour at 550 °C to ~8 kΩ after 5 hours, and the 650 °C–1 h sample yields a comparable value to the 550 °C–5 h condition, reflecting enhanced graphitic ordering and electrical conductivity in the carbon shell.

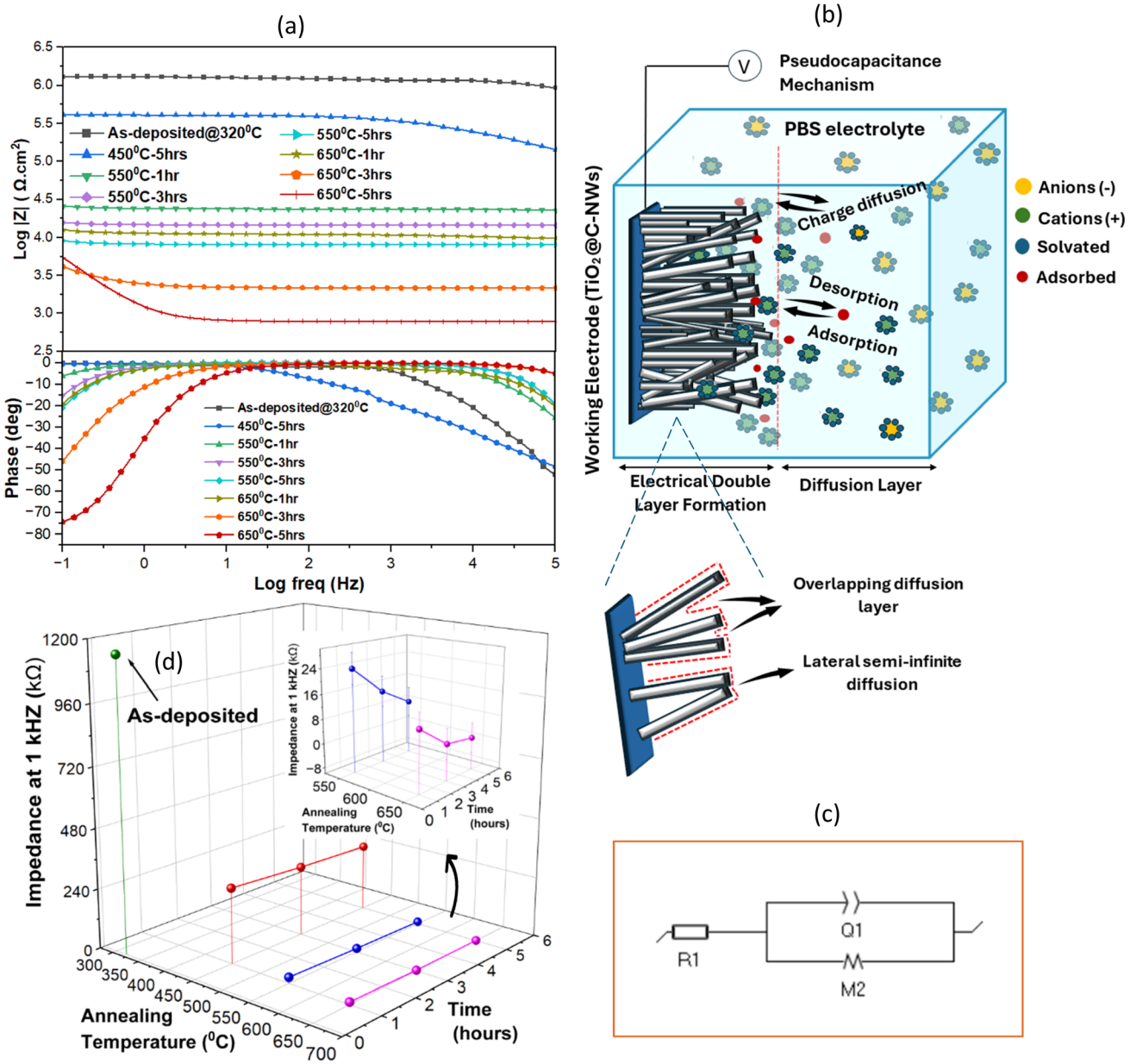

Fig. 7 EIS performance of as-deposited TiO_2@C core–shell NWs and *in situ* annealed at 450 °C, 550 °C, and 650 °C for varying duration showing (a) the Bode and phase plots, (b) schematic illustration of electrolyte diffusion mechanism, (c) equivalent circuit of TiO_2@C core–shell NWs *in situ* annealed at 650 °C for 3 hours, (d) impedance values of treated samples at 1 kHz.

At frequencies below ~120 Hz, the impedance magnitude of the 550 °C and 650 °C annealed samples begins to rise (see enlarged Bode plots in Fig. S7), indicating that capacitive effects are beginning to overtake the pure resistance. From the phase plot, the knee frequency, where the phase angle departs from 0° and capacitive behavior emerges, is 0.37 Hz, 0.72 Hz, and 1 Hz for the 550 °C samples annealed for 1, 3, and 5 hours, respectively, and 1.39 Hz for the 650 °C–1 h sample; at 0.1 Hz, the phase angle shifts negatively between −18° and −25°, indicating the presence of both resistive and capacitive components. Such limited phase shift is characteristic of a non-ideal electrochemical double-layer capacitance at the carbon–electrolyte interface and suggests that, although capacitive charging has initiated, it is not yet dominant, likely due to incomplete graphitization and residual resistive pathways in the carbon shell.

When annealing is extended at 650 °C to 3 and 5 hours, the knee frequency rises to 7.17 Hz and 19.27 Hz, respectively, and the phase angle at 0.1 Hz reaches −45° and −75°, demonstrating stronger capacitive response, enhanced ion accumulation, and improved charge-storage capability. These earlier transitions toward capacitive behavior reflect more efficient interfacial charging afforded by higher graphitic ordering and electrical conductivity. Nevertheless, these optimized samples still exhibit slow capacitive transitions. This may indicate the existence of ion-diffusion resistance within the densely packed nanowire array (see Fig. 7(b)). When the inter-wire spacing or pore radii approach a few Debye lengths, the diffusion layers from adjacent surfaces begin to overlap, collapsing two diffusion regions into one highly confined, charged zone.[46] This overlap both reduces the effective double-layer capacitance and forces ions to traverse a constricted environment, thereby raising the ion-transport resistance. As illustrated in the enlarged image of Fig. 7(b), overlapping electrical double layers limit the accessible surface area for charge storage and delay the onset of capacitive dominance to much lower frequencies. This behavior is clearly reflected in the Nyquist plot (Fig. S8); all 550 °C–annealed samples (1, 3, 5 hours) and the 650 °C–1 h samples exhibit an (incomplete) high-frequency semicircle, truncated by the 1 MHz limit of our instrument, that marks ions transport resistance at the TiO_2–TiC–C interface. As the frequency falls into the 20–100 Hz range, each curve departs away from its semicircle into an approximately 45°-sloped "diffusion" line, signaling that ion transport within the tightly packed nanowire structure has become diffusion-limiting. Even the 650 °C sample annealed for 3 and 5 hours, which display much smaller semicircles (R_{ct} dropping to $\lesssim$1 kΩ), still show pronounced diffusion tails at low frequencies. This confirms that, despite dramatically reduced interfacial barriers, mass transport through the electrolyte–nanowire network remains the dominant impedance contributor.

To quantify these effects, we fitted the Nyquist plot of the 650 °C–3 h sample to the equivalent circuit shown in Fig. 7(c), consisting of a series resistance (R_1) in series with a parallel combination of a constant-phase element (Q_1) and a finite-length diffusion element (M_2). The series resistance, $R_1 \approx$ 3.76 kΩ, represents the uncompensated ohmic drop at the electrolyte–nanowire interface and defines the high-frequency intercept on the real axis. Q_1 (magnitude $\approx 3.85 \times 10^{-4}$ F $s^{(n-1)}$, exponent $n \approx 0.84$) accounts for the non-ideal, semi-porous double-layer and semi-infinite diffusion behaviour at the rough nanowires tips, with $n < 1$ reflecting a distributed double layer over an undulating surface rather than a smooth planar film. The finite-length diffusion element M_2 (with a diffusion resistance of ≈10.4 kΩ and a characteristic time constant $\tau \approx 1.50$ s) quantifies the bounded, diffusion-limited ion transport responsible for the low-frequency diffusion-tail by capturing how overlapping diffusion layers in the high-density, low-gap nanowire structure constrain ion flux from the bulk electrolyte into the interstices. Together, these fitted values confirm that, despite significantly lowered interfacial barriers at this condition, ion transport through the densely packed nanowire array, exacerbated by overlapping double layers, remains the primary impedance contributor.

Impedance at 1 kHz is also an important benchmark for evaluating neural recording electrodes, as it falls within the frequency range of neural signals.[47] Based on the Bode plots, the 1 kHz impedance values were extracted and are presented in Fig. 7(d). A clear downward trend in impedance is observed with increasing annealing temperature and duration. At 1 kHz the as-deposited carbon showed a relatively high impedance of 1.1 MΩ after which it largely decreased to 300 kΩ at 450 °C after 1 hour, with a modest further decrease to ~267.2 kΩ after 5 hours. At 550 °C, the improvement becomes more pronounced, with impedance reducing from 23.8 kΩ (1 hour) to 8.2 kΩ (5 hours), indicating enhanced carbon ordering. The most substantial reduction occurs at 650 °C, where the impedance drops to 770 Ω after 5 hours, representing nearly a three-order-of-magnitude decrease compared to the as-deposited state. A secondary minimum of 2.1 kΩ is also observed at 3 hours. These results reflect a progressive enhancement in graphitization, increased sp^2 carbon content, and improved electrical pathways within the carbon shell, all contributing to lower charge transfer resistance and improved electrochemical performance. Importantly, achieving these properties at ≤650 °C represents a significant advantage over conventional CVD processes that require temperatures >1000 °C. The reduced thermal budget enables conformal carbon deposition on thermally sensitive substrates and nanostructures, such as FTO- or ITO-coated glass used in neural MEA platforms, that would otherwise deform or degrade at higher temperatures. Moreover, noble-metal nanostructures like Au, which serve as effective scaffolds for neural interfaces due to their high conductivity and biocompatibility, are prone to dewetting or coarsening at temperatures starting from 700 °C.[48] By maintaining the synthesis temperature at or below 650 °C, these nanostructures remain morphologically stable and can be functionalized with a conformal carbon shell. It is believed that this approach preserves their structural and electrochemical integrity while enhancing overall device performance.

3.4.3 Electrochemical stability test. Another critical property of neural electrode materials, particularly when interfacing with biological tissue, is their electrochemical stability, the ability to maintain structural, compositional, and capacitive

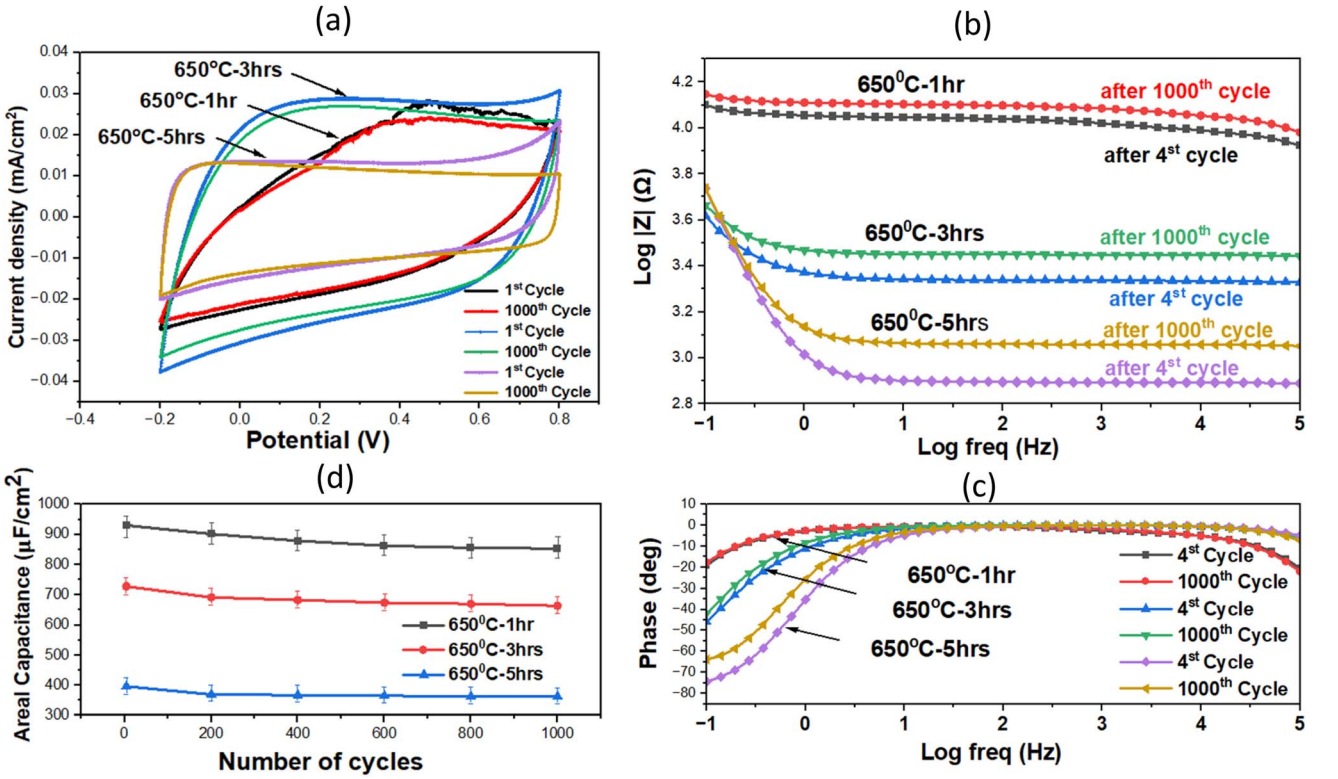

Fig. 8 (a) CV performance of TiO_2@C core–shell NWs *in situ*-annealed at 650 °C for 1, 3, and 5 hours and their corresponding (b) Bode plots and (c) phase plots undergoing 1000 cycles, and (d) areal capacitance values across 1000 cycles.

integrity during prolonged operation. To evaluate this, we investigated the electrochemical cyclability of TiO_2@C-NWs annealed at 650 °C for 1, 3, and 5 hours. These conditions were selected based on their previously demonstrated superior electrochemical performance, allowing us to assess how annealing duration affects long-term stability. Each sample was subjected to 1000 continuous CV cycles at a scan rate of 100 mV s^{-1} in PBS. Fig. 8(a)–(c) compares the 4th and final CV cycles for each sample, along with their corresponding Bode and phase plots, respectively. The near-identical CV profiles before and after cycling across all samples indicate excellent electrochemical and morphological stability, with no significant degradation in capacitive behavior. This stability confirms the robustness of the TiO_2@C-NWs under prolonged electrochemical stress. As shown in Fig. 8(d) all three samples demonstrate high capacitance retention of approximately 92%, reinforcing their durability. However, changes in impedance and phase an gle reveal subtle differences in performance. The total impedance $|Z|$ at 1 kHz increased by 22.7%, 32.4%, and 48.6% for the 1, 3, and 5-hour annealed samples, respectively. While all values remain within acceptable limits, the increasing trend of impedance suggests that longer annealing may introduce microstructural changes, such as carbon overgrowth or slight delamination, or an increase in accumulation of surface ions on the electrode, that impacts interfacial resistance over multiple cycles. Additionally, phase angle shifts at low frequencies provide further insight, with the sample annealed for 5 hours showing a notable change in phase shift from −75° to −63°, indicating a decrease in ideal capacitive behavior.

3.4.4 Effect of varying scan rate. In practical neural stimulation applications, selecting an appropriate CV scan rate is critical, as it affects several factors, including the neural tissue response, the specific electrode material, and most importantly, the electrode's ability to provide a reliable capacitive response. Therefore, it is essential to evaluate the electrode material's capacitive behavior across a range of scan rates to ensure electrochemical stability and reversibility. Typically, scan rates between 10 and 100 mV s^{-1} are deemed optimal for neural stimulation studies, balancing accurate characterization of electrochemical behavior with effective charge transfer. In this study, we assessed the electrochemical performance of TiO_2@C nanowires annealed at 650 °C for 3 hours over a range of scan rates from 5 to 200 mV s^{-1} (Fig. 9(a)). The CV curves exhibit quasi-rectangular shapes across all scan rates, indicating good capacitive behavior and electrochemical stability of the nanowire film. As shown in Fig. 9(b), the areal capacitance decreases from approximately 2040 μF cm^{-2} at 5 mV s^{-1} to about 1250 μF cm^{-2} at 200 mV s^{-1}. This decline in capacitance with increasing scan rate is attributed to limited ion diffusion into the electrode's porous structure at higher scan rates, which restricts access to the inner active surface area. Conversely, lower scan rates allow ions sufficient time to penetrate deeper into the electrode material, enhancing charge storage. Importantly, the areal capacitance approaches a steady value at high scan rates, indicating the robustness and suitability of the TiO_2@C-NWs

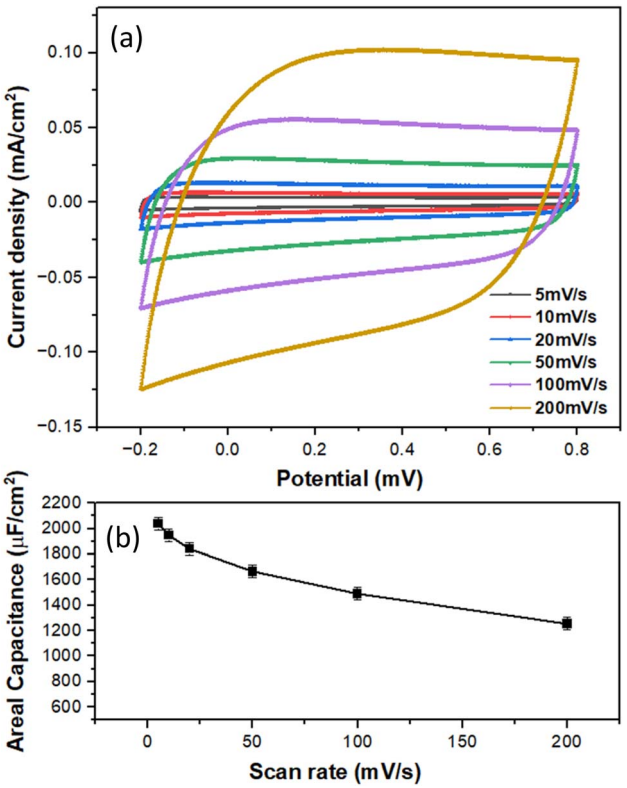

Fig. 9 (a) CV performance of TiO_2@C core–shell NWs *in situ*-annealed at 650 °C for 3 hours measured at various scan rate, and (b) corresponding plot of areal capacitance *vs.* scan rate.

electrode for neural interface applications, potentially including dynamic stimulation protocols requiring rapid charge delivery.

3.5 Biocompatibility test

Evaluating the biocompatibility of the synthesized TiO_2@C-NWs is critical for validating their suitability as cellular interface materials. To assess their cytocompatibility, the human cell line HeLa was selected since it is a well-established and readily available cell-culture model for studying cellular responses to novel materials.[49,50] These cells were cultured directly on TiO_2@C-NWs surfaces and carbon films deposited under identical conditions on FTO/glass. These were compared to a standard tissue culture 35 mm μ-dishes, serving as a control. Key biological metrics, cell viability (live/dead assay), cellular distribution, and proliferation, were examined to understand how the nanostructured and planar carbon surfaces influence cell behavior. As shown in Fig. 10, all samples exhibited high cell viability, with no significant difference between TiO_2@C-NWs, TiO_2@C-film and the control, indicating the absence of cytotoxic effects from either the carbon coating or the underlying nanostructured substrate. Notably, both TiO_2@C-NWs and TiO_2@C-film supported higher cell densities than the control, suggesting enhanced cell adhesion and substrate compatibility, likely attributed to increased surface area or favorable surface chemistry introduced by the carbon layer. Although the TiO_2@C-NWs group exhibited a slightly lower cell density than the TiO_2@C-film, it still demonstrated superior performance compared to the control. While the film offers

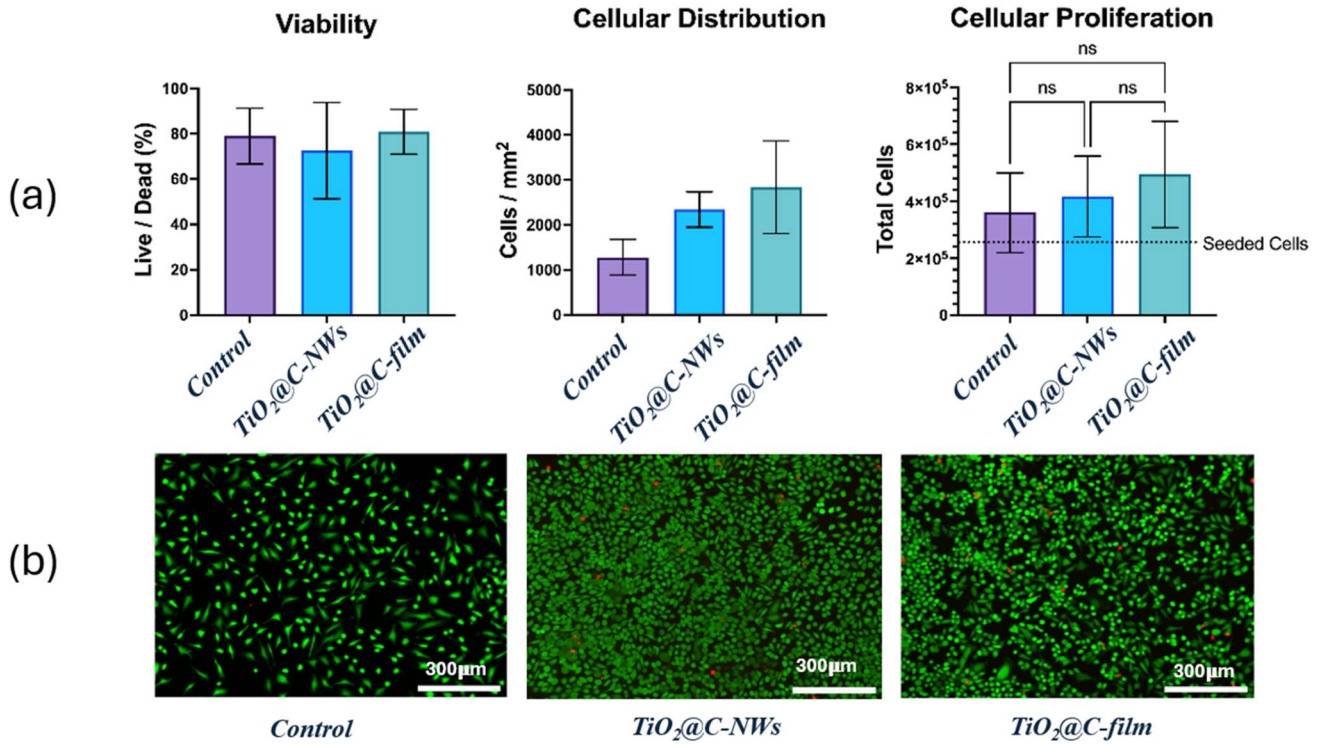

Fig. 10 Biocompatibility assessment TiO_2@C-NWs *vs.* TiO_2@C-film using HeLa Cells. (a) Quantitative analysis demonstrating cell viability as live/dead percentage, cellular distribution (cells per mm^2), and total cell proliferation. (b) Representative live/dead fluorescence microscopy images.

a more continuous and uniform surface for cell spreading, the nanowires introduce distinct morphological cues that can stimulate localized adhesion and cellular anchorage through filopodia. Wang Yu *et al.*[51] showed that TiO_2 nanotube surfaces with diameters of 70–100 nm promoted longer filopodia and greater cell proliferation due to enhanced protein adsorption and the presence of sharp convex features. A similar mechanism may be at play on the TiO_2@C-NW surfaces, where nanoscale texture encourages filopodial interaction. Proliferation analysis revealed that total cell counts after the culture period exceeded the initially seeded cell number for all conditions, confirming that the materials not only support survival but actively permit cell growth. While the carbon film showed a marginally higher cell count, differences among all three groups were statistically insignificant. Fluorescence microscopy further confirmed these findings, showing well-spread live cells with minimal dead staining across all samples. Overall, these results demonstrate that the TiO_2@C-NWs are biocompatible, non-cytotoxic, and capable of supporting cellular activity comparable to conventional culture substrates. Building on these promising outcomes, future studies will expand the biological evaluation to neural-specific models, with the aim of assessing parameters such as neuronal adhesion, neurite extension, and long-term interface stability, thereby strengthening the translational relevance of TiO_2@C-based architectures for neural electrode applications.

4 Conclusion

This study explored the electrochemical performance and biocompatibility of TiO_2@C core–shell nanowires deposited at 320 °C using PECV D, followed by *in situ* annealing at 450 °C, 550 °C, and 650 °C for durations of 1, 3, and 5 hours. The goal was to evaluate their potential as electrode interface materials for neural applications. The results revealed a substantial enhancement in electrochemical properties with increasing annealing temperature and duration, with the areal capacitance increasing from 1.93 μF cm^{-2} (450 °C, 5 h) to a peak of 874.4 μF cm^{-2} (650 °C–3 h), accompanied by a significant reduction in electrochemical impedance at 1 kHz from ∼267.2 kΩ to 2.1 kΩ. This enhancement was primarily attributed to: (1) an increased sp^2/sp^3 carbon ratio, indicating higher graphitization and improved electrical conductivity, and (2) the formation of Ti^{3+}-containing phases such as TiC, as confirmed by EELS, which facilitate defect-assisted charge transport. Therefore, this work demonstrates the fabrication of electrochemically active, low-impedance TiO_2@C core–shell NWs with ultra-thin (∼5 nm) carbon coatings, using a low-temperature PECVD and annealing approach. The approach presents a promising pathway for engineering next-generation neural interface materials, particularly where thermal budget constraints are critical. Future investigations should focus on biological studies with neural cell cultures to evaluate neuronal adhesion, neurite outgrowth, and long-term biosafety on TiO_2@C interfaces. In parallel, systematic tuning of the carbon shell thickness, as well as strategies to modulate the sp^2/sp^3 carbon ratio through controlled doping, represent promising avenues for further optimization. Progressing toward *in vivo* validation in animal models and the fabrication of miniaturized neural electrode prototypes will be essential steps to advance this material platform toward translational and clinical applications.

Author contributions

Roaa Sait conceived and initiated the research project, designed the experimental workflow, led data analysis, developed the manuscript structure, and wrote the majority of the manuscript including the final conclusions. Raghad Alzahrani performed the hydrothermal growth of TiO_2 nanowires and conducted the core experimental procedures. She also contributed to partial data analysis, helped in shaping the research concept, and assisted in formulating the final conclusions. Nabeel Aslam was responsible for performing the plasma-enhanced chemical vapor deposition (PECVD) experiments and provided key materials and technical support for the coating process. Shofarul Wustoni conducted the electrochemical measurements, including cyclic voltammetry and impedance spectroscopy, and carried out the corresponding data analysis and interpretation. Camelia Florica acquired and analyzed scanning electron microscopy (SEM) images, and contributed to the evaluation of nanowire morphology and surface coatings. Andrea Diaz-Gaxiola handled all cell culture experiments, including the preparation, maintenance, and testing of cellular interactions with the samples, and analyzed the biological response data. Georgian Melinte performed STEM and EELS, contributing to the structural and compositional analysis of the coated nanowires. Yaping Zhang conducted Raman spectroscopy measurements and performed spectral analysis to evaluate carbon structure and crystallinity. Youyou Yuan carried out XRD experiments and analyzed the crystalline phase composition of the nanomaterials. Mohammed Nejib Hedhili performed XPS characterization and analyzed surface chemical states and elemental compositions. Sridhar Govindarajan assisted in the interpretation and analysis of electrochemical data, supporting comparison and validation of sample performance. Ahad Syed provided essential materials for the experiments and contributed to project oversight and technical supervision throughout the study. Imed Eddine-Gallouzi supervised the biological testing procedures and assisted in managing the supply and selection of materials used in the study. Sahika Inal supported the acquisition and characterization of electrochemical materials and assisted with technical analysis of performance data. Hala Aljawhari contributed to the procurement of synthesis materials and offered supervisory support during experimental planning and execution.

Conflicts of interest

There are no conflicts to declare.

Data availability

The data that support the findings of this study are available from the corresponding author upon reasonable request.

Supplementary information: comprehensive characterization data supporting the development of TiO_2@C core–shell nanowires. Fig. S1 presents STEM images and corresponding EELS elemental profile for the as-deposited and annealed samples at 450 °C, 550 °C, and 650 °C (5 h). Fig. S2 displays top-region EELS spectra with high-resolution C K-edge insets to assess bonding environments. Fig. S3 further confirms carbon coating *via* EELS mapping of as-deposited and 650 °C (3 h) annealed samples. Fig. S4 presents XRD patterns evolution with annealing. Fig. S5 contains Raman spectra of pristine TiO_2 NWs. Fig. S6 provides XPS survey scans of annealed samples for 3 hours. Fig. S7 and S8 show Bode and Nyquist impedance plots, respectively, for samples annealed under different conditions. See DOI: https://doi.org/10.1039/d5ra05460e.

Funding

The authors would like to acknowledge the General Authority for Defense Development (GADD) in Saudi Arabia for funding this research through project number (GADD_2024_01_164).

Acknowledgements

The authors gratefully acknowledge the technical support provided by the Nanofabrication Core Laboratories at King Abdullah University of Science and Engineering.

References

1 H. Li, J. Wang and Y. Fang, Recent developments in multifunctional neural probes for simultaneous neural recording and modulation, *Microsyst. Nanoeng.*, 2023, **9**, 4.
2 B. Karamian, N. Siegel, B. Nourie, M. Serruya, R. Heary, J. Harrop and A. Vaccaro, The role of electrical stimulation for rehabilitation and regeneration after spinal, *J. Orthop. Traumatol.*, 2022, **23**(1), 2.
3 N. Wu, S. Wan, S. Su, H. Huang, G. Dou and L. Sun, Electrode materials for brain–machine interface: A review, *InfoMat*, 2021, **3**(11), 1174–1194.
4 A. Bajo, J. Rosa, A. Mayorga, B. Rodilla, A. Núñez, E. Benayas, P. Ocón, L. Perez, J. Camarero, R. Miranda, M. T. González, J. Aguilar, E. Dolado and M. Serrano, Nanostructured gold electrodes promote neural maturation and network connectivity, *Biomaterials*, 2021, **279**, 121186.
5 C. Boehler and S. T, Nanostructured Platinum Grass Enables Superior Impedance reduction for Neural Microelectrodes, *Biomaterials*, 2015, **67**, 346–353.
6 A. Bajo, B. Rodilla, I. Calaresu, A. Núñez, A. Mayorga, D. Scaini, L. Pérez, J. Camarero, R. Miranda, E. Dolado, M. González, L. Ballerini and M. Serrano, Interfacing Neurons with Nanostructured Electrodes Modulates Synaptic Circuit Features, *Adv. Biosyst.*, 2020, **4**(9), 2000117.
7 M. Vafaiee, R. Mohammadpour, M. Vossoughi, E. Asadian, M. Janahmadi and P. Sasanpour, Carbon Nanotube Modified Microelectrode Array for Neural Interface, *Front. Bioeng. Biotechnol.*, 2021, **8**, 582713.
8 H. Su, C. Lin, Y. Chen, C. Chen, S. Yeh, W. Fang, H. Chen, D. Yao, Y. Chang and T. Yew, A cone-shaped 3D carbon nanotube probe for neural recording neural recording, *Biosens. Bioelectron.*, 2010, **26**(1), 220–227.
9 K. Miki, T. Watanabe and S. Koh, Electrochemical Characterization of CVD-Grown Graphene for Designing Electrode/Biomolecule Interfaces, *Crystals*, 2020, **10**(4), 241.
10 M. Vomero, E. Castagnola, F. Ciarpella, E. Maggiolini, N. Goshi, E. Zucchini, S. Carli, L. Fadiga, S. Kassegne and D. Ricci, Highly Stable Glassy Carbon Interfaces for Long-Term Neural Stimulation and Low-Noise Recording of Brain Activity, *Sci. Rep.*, 2017, **7**, 40332.
11 E. Castagnola, E. Robbins, B. Wu, M. Pwint, G. Raghav, T. Karni and X. Cui, Flexible Glassy Carbon Multielectrode Array for In Vivo Multisite Detection of Tonic and Phasic Dopamine Concentrations, *Biosensors*, 2022, **12**, 540.
12 W. Tong, K. Fox, A. Zamani, A. Turnley, K. Ganesan, A. Ahnood, R. Cicione, H. Meffin, S. Prawer, A. Stacey and D. Garrett, Optimizing growth and post treatment of diamond for high capacitance neural interfaces, *Biomaterials*, 2016, **104**, 32–42.
13 R. Bharti, P. Kaushik, S. Naik, A. Thakur, M. Verma and R. Sharma, Low Temperature Synthesis of Carbon Nanostructures, in *Handbook of Functionalized Carbon Nanostructures*, Springer, Cham, 2024, pp. 1–45.
14 S. Sharma, Glassy Carbon: A Promising Material for Micro- and Nanomanufacturing, *Materials*, 2018, **11**(10), 1857.
15 W. Huang, S.-P. Wang, T.-Y. Wang, W.-L. Chen and P.-C. Chen, Space-controllable TiO2@IrO2 core-shell nanotube array as a bio-interface electrode, *Surf. Coat. Technol.*, 2022, **435**, 128271.
16 M. Kim, Y. Lee, S.-J. Kim, B.-M. Hwang, H. Park, E. Hwang, G. Cao and K. Park, Improved Lithium Ion Behavior Properties of TiO2@Graphitic-like Carbon Core@Shell Nanostructure, *Electrochim. Acta*, 2014, **147**, 241–249.
17 X. Wang, C. Guan, S. Leimeng, R. Susantyoko, H. Fan and Q. Zhang, Highly stable and flexible Li-ion battery anodes based on TiO2 coated 3D carbon nanostructures, *J. Mater. Chem. A*, 2015, **3**, 15394–15398.
18 L. Hou, H. Hua, H. Cao, S. Zhu and C. Yuan, A core–shell TiO2@C nano-architecture: facile synthesis, enhanced visible photocatalytic performance and electrochemical capacitance, *Roy. Soc. Chem.*, 2015, **5**, 62424–62432.
19 J. Lee, S. Han, J. Kim, Y. Lee, A.-R. Ko, B. Roh, I. Hwang and K. Park, TiO2@carbon core–shell nanostructure supports for platinum and their use for methanol electrooxidation, *Carbon*, 2010, **48**(8), 2290–2296.
20 A. Kumar, A. Madaria and C. Zhou, Growth of Aligned Single-Crystalline Rutile TiO2 Nanowires on Arbitrary Substrates and Their Application in Dye-Sensitized Solar Cells, *J. Phys. Chem. C*, 2010, **114**(17), 7787–7792.
21 C. Yuan, B. Gao and X. Zhang, Electrochemical capacitance of NiO/Ru0.35V0.65O2 asymmetric electrochemical capacitor, *Power Sources*, 2007, **173**(1), 606–612.
22 I. 10993-5, *Biological Evaluation of Medical Devices. Part 5: Tests for in Vitro Cytotoxicity*, International Organization for Standardization, Geneva, 2009.

23 I. Watanabe and T. Okumura, Annealing Behavior of Amorphous C:H Films prepared by glow discharge decompoisiton of CH4 and H2, *Jpn. J. Appl. Phys.*, 1986, **25**(12), 1851–1854.
24 S. Paul and F. Clough, Substrate Sensitivity of the Adhesion and Material Properties of RF-PECVD Amorphous Carbon, *MRS Online Proc. Libr.*, 1999, **558**, 149–154.
25 D. Piliptsou, X. Jiang, A. Chaus, A. Rogachev and L. Morovic, Influence of annealing on the structure and properties of carbon coatings containing Ti and TiN layers, *Diamond Relat. Mater.*, 2023, **135**, 109890.
26 L. Ponsonnet, C. Donnet, K. Varlot, J. Martin, A. Grill and V. Patel, EELS analysis of hydrogenated diamond-like carbon films, *Thin Solid Films*, 1998, **319**, 97–100.
27 S. Reich and C. Thomsen, Raman spectroscopy of graphite, *Philos. Trans. R. Soc., A*, 2004, **362**(1824), 2271–2288.
28 S. Porto, P. Fleury and T. Damen, Raman Syectra of TiO2, MgF2, ZnF2, FeF2, and MnF2, *Phys. Rev.*, 1967, **154**, 522.
29 H. Ma, J. Yang, Y. Dia, Y. Zhang, B. Lu and G. Ma, Raman study of phase transformation of TiO2 rutile single crystal irradiated by infrared femtosecond laser, *Appl. Surf. Sci.*, 2007, **253**, 7497–7500.
30 L. Lin, M. Lai, H. Li, F. Tian, Y. Chen, J. Sun and M. Lin, Investigation of carbon deposition induced by pyrolytic decomposition of ethylene, *Roy. Soc. Chem.*, 2017, **7**, 29639.
31 R. Kaindl, G. Jakopic, R. Resel, J. Pichler, A. Fian, E. Fisslthaler, W. Grogger, B. Bayer, R. Fischer and W. Waldhauser, Synthesis of graphene-layer nanosheet coatings by PECVD, *Mater. Today: Proc.*, 2015, **2**, 4247–4255.
32 B. Baboukani, Z. Ye and K. Komvopoulos, Enhancing Graphene Growth in Carbon Ultrathin Films by Tuningthe Ion Kinetic Energy During Film Deposition onto a CatalystSublayer, *J. Phys. Chem.*, 2024, **128**, 15141–15150.
33 D. Schuepfer, F. Badaczewski, J. Guerra-Castro, D. Hofmann, C. Heiliger, B. Smarsly and P. Klar, Assessing the structural properties of graphitic and non-graphitic carbons by Raman spectroscopy, *Carbon*, 2020, **161**, 359–372.
34 C. Casiraghi, A. Ferrari and J. Robertson, Raman spectroscopy of hydrogenated amorphous carbons, *Phys. Rev.*, 2005, **72**, 085401.
35 H. Wang, Y. Wang, T. Li, S. Wu and L. Xu, Gradient distribution of radial structure of PAN-based carbon fiber treated by high temperature, *Prog. Nat. Sci.:Mater. Int.*, 2014, **24**(1), 31–34.
36 B. Lesiak, L. Kövér, J. Tóth, J. Zemek, P. Jiricek, A. Kromka and N. Rangam, C sp2/sp3 hybridisations in carbon nanomaterials – XPS and (X)AES study, *Appl. Surf. Sci.*, 2018, **452**, 223–231.
37 M. Singh, A. Yada, S. Kumar and P. Agarwal, Annealing induced electrical conduction and band gap variation in thermally reduced graphene oxide films with different sp2/sp3 fraction, *Appl. Surf. Sci.*, 2015, **326**, 236–242.
38 Q. Wang, M. Li and Z. Wang, Supercapacitive performance of TiO_2 boosted by a unique porous TiO_2/Ti network and activated Ti^{3+}, *RSC Adv.*, 2019, **9**(11), 6267–6275.
39 J. Zhi, H. Cui, Z. Wang and F. Huang, Surface confined titania redox couple for ultrafast energy storage, *Mater. Horiz.*, 2018, **5**, 691–698.
40 T. Mathis, N. Kurra, X. Wang, D. Pinto, P. Simon and Y. Gogotsi, Energy Storage Data Reporting in Perspective—Guidelines for Interpreting the Performance of Electrochemical Energy Storage Systems, *Adv. Energy Mater.*, 2019, **9**, 1902007.
41 Y. Dong, X. Dong, D. Zhu, Y. Yang, C. Luo, Y. Li and J. Li, Combination of multiple active sites in N, O co-doped defective carbon materials for high performance aqueous supercapacitors, *Nano Sel.*, 2023, 1–8.
42 F. Mangolini, F. Rose, J. Hilbert and R. Carpick, Thermally induced evolution of hydrogenated amorphous carbon, *Appl. Phys. Lett.*, 2013, **103**, 161605.
43 N. Dwivedi, S. Kumar, H. Malik, C. Rauthan and O. Panwar, Correlation of sp3 and sp2 fraction of carbon with electrical, optical and nano-mechanical properties of argon-diluted diamond-like carbon films, *Appl. Surf. Sci.*, 2011, **257**, 6804–6810.
44 S. Chugh, R. Mehta, N. Lu, F. D. Dios, M. Kim and Z. Chen, Comparison of graphene growth on arbitrary non-catalytic substrates using low-temperature PECVD, *Carbon*, 2015, **93**, 393–399.
45 H. Zanin, P. May, R. Harniman, T. Risbridger, E. Corat and D. Fermin, High surface area diamond-like carbon electrodes grown on vertically aligned carbon nanotubes, *Carbon*, 2015, **82**, 288–296.
46 N. Kemp, A Tutorial on Electrochemical Impedance Spectroscopy and Nanogap Electrodes for Biosensing Applications, *IEEE Sens. J.*, 2021, **21**(20), 22232–22245.
47 J. Williams, J. Hippensteel, J. Dilgen, W. Shain and D. Kipke, Complex impedance spectroscopy for monitoring tissue responses to inserted neural implants, *J. Neural. Eng.*, 2007, **4**, 410–423.
48 B. Schaefer, J. Cheung, J. Ihlefeld, J. Jones and V. Nagarajan, Stability and dewetting kinetics of thin gold films on Ti, TiOx and ZnO adhesion layers, *Acta Mater.*, 2013, **61**(20), 7841–7848.
49 H. Le, J. Kim, J. Park and S. Cho, A Review of Electrical Impedance Characterization of Cells for Label-Free and Real-Time Assays, *BioChip J.*, 2019, **13**, 295–305.
50 K. Koo, C. Kim, F. Ju, H. Kim, C. Kim and T. Kim, Recent Advances in Electrochemical Biosensors for Monitoring Animal Cell Function and Viability, *Biosensors*, 2022, **12**(12), 1162.
51 Y. Wang, C. Wen, P. Hodgson and Y. Li, Biocompatibility of TiO2 nanotubes with different topographies, *J. Biomed. Mater. Res., Part A*, 2014, **102**(3), 743–751.